

# Correction Method for the Readout Saturation of the DAMPE Calorimeter

Chuan Yue<sup>a,\*</sup>, Peng-Xiong Ma<sup>a,b,\*</sup>, Margherita Di Santo<sup>c,d</sup>, Li-Bo Wu<sup>e</sup>,  
 Francesca Alemanno<sup>f,g</sup>, Paolo Bernardini<sup>c,d</sup>, Dimitrios Kyratzis<sup>f,g</sup>, Guan-Wen  
 Yuan<sup>a,b</sup>, Qiang Yuan<sup>a,b</sup>, Yun-Long Zhang<sup>e</sup>

<sup>a</sup>*Key Laboratory of Dark Matter and Space Astronomy, Purple Mountain Observatory,  
 Chinese Academy of Sciences, Nanjing 210008, China*

<sup>b</sup>*School of Astronomy and Space Science, University of Science and Technology of China,  
 Hefei 230026, China*

<sup>c</sup>*Dipartimento di Matematica e Fisica E. De Giorgi, Università del Salento, I-73100 Lecce,  
 Italy*

<sup>d</sup>*Istituto Nazionale di Fisica Nucleare (INFN) Sezione di Lecce, I-73100 Lecce, Italy*

<sup>e</sup>*State Key Laboratory of Particle Detection and Electronics, University of Science and  
 Technology of China, Hefei 230026, China*

<sup>f</sup>*Gran Sasso Science Institute (GSSI), Via Iacobucci 2, I-67100 L'Aquila, Italy*

<sup>g</sup>*Istituto Nazionale di Fisica Nucleare (INFN) -Laboratori Nazionali del Gran Sasso,  
 I-67100 Assergi, L'Aquila, Italy*

---

## Abstract

The DARK Matter Particle Explorer (DAMPE) is a space-borne high energy cosmic-ray and  $\gamma$ -ray detector which operates smoothly since the launch on December 17, 2015. The bismuth germanium oxide (BGO) calorimeter is one of the key sub-detectors of DAMPE used for energy measurement and electron-proton identification. For events with total energy deposit higher than decades of TeV, the readouts of PMTs coupled on the BGO crystals would become saturated, which results in an underestimation of the energy measurement. Based on detailed simulations, we develop a correction method for the saturation effect according to the shower development topologies and energies measured by neighbouring BGO crystals. The verification with simulated and on-orbit events shows that this method can well reconstruct the energy deposit in the saturated BGO crystal.

*Keywords:* DAMPE, BGO Calorimeter, Readout Saturation, Cosmic-rays

---

\*Corresponding author

*Email addresses:* yuechuan@pmo.ac.cn (Chuan Yue), mapx@pmo.ac.cn (Peng-Xiong Ma)

## 1. Introduction

Measurements of the energy spectra of various cosmic ray (CR) nuclei are the key to understanding the origin, propagation, and interaction of these energetic particles [1–3]. Current measurements carried out by magnetic spectrometer experiments reach very high precision up to TV rigidities [4]. At even higher energies, direct measurements by calorimeter experiments show interesting hints that the spectra of CR nuclei may have complicated structures [5–7]. However, these results are still subject to relatively large uncertainties, due to either limited statistics or large systematic uncertainties. Improved measurements are essential and necessary for addressing those important questions of CR physics.

The DArk Matter Particle Explorer (DAMPE; [8, 9]) is an orbital mission for precision measurements of CR nuclei, electron/positrons, and  $\gamma$ -ray, supported by the strategic priority science and technology projects in space science of the Chinese Academy of Science. It was launched into a sun-synchronous orbit at an altitude of 500 km on December 17, 2015, and has been working smoothly for more than 4 years since then. The scientific payload of DAMPE consists of four sub-detectors, including a Plastic Scintillator strip Detector (PSD; [10, 11]), a Silicon-Tungsten tracker-converter (STK; [12, 13]), a BGO imaging calorimeter (BGO; [14, 15]), and a NeUtron Detector (NUD; [16]). These four sub-detectors work cooperatively to enable good measurements of charge, track, energy and particle-id of each incident particle [17–19]. Precise spectral measurements regarding electrons plus positrons [20] and protons [21] in extended energy intervals, reveal interesting features and shed new light on the understandings of CR physics, while improving the constraints on dark matter models [22–25]. The  $\gamma$ -ray identification technique [26] and analysis tool [27] have also been developed, with preliminary results [28].

The BGO calorimeter is the main sub-detector for energy measurement, which is designed as a total-absorption electromagnetic calorimeter of about

31.5 radiation length and 1.6 nuclear interaction length. It is composed of 14 layers, each layer consists of 22 BGO crystals ( $25 \times 25 \times 600 \text{ mm}^3$ ) placed orthogonally in two dimensions [14]. The fluorescence signal of each BGO crystal is read out by two PMTs mounted on both ends. This design provides two independent energy measurements. Apart from measuring the energy deposits of the cascade showers produced by incident particles, the calorimeter images their shower developments, thereby serving as a hadron/lepton discriminator [20].

At the very-high-energy end of DAMPE's capability, saturations of the low-gain readouts appear<sup>1</sup>, which affect the precise measurement of the particle energy. For most of the saturated events, there are no more than one BGO crystal in the same layer showing the saturation effect. In this work, we develop a method to correct the saturated readout for those events, which is helpful in reconstructing the proper energy deposits of them. Applying such corrections would enable us to significantly enlarge the measurable energy ranges of CR nuclei.

## 2. BGO Readout Saturation

To fulfil the requirement of a wide energy coverage, from 5 GeV to 10 TeV for  $e^\pm/\gamma$  and up to 100 TeV for nuclei, the scintillation light signal of each BGO crystal is read out from three different sensitive dynodes 2, 5, and 8 (Dy2, Dy5, and Dy8) of the PMTs, which corresponds to low-gain, medium-gain, and high-gain channels, respectively [29]. The response ratios of adjacent dynodes, i.e. Dy8/Dy5 and Dy5/Dy2, are carefully calibrated using high-energy shower events collected on orbit, which show good linear correlations and maintain stability over time [30]. Non-linearity effect from the conversion of the ionization energy to the light yield [31] has not been found for electrons up to a few TeV energies. However, for each PMT dynode, an upper limit of the ADC readout has been

---

<sup>1</sup>For protons and helium nuclei, the saturation may happen for deposited energies higher than  $\sim 20 \text{ TeV}$ .

set beyond which the readout is discarded on orbit. The PMTs on the two ends of one BGO crystal (named S0 and S1) are coupled to the BGO bar with two different optical filters. The filter on the S1 end has a factor of  $\sim 5$  times attenuation with respect to the one on the S0 end, thereby the upper limit of the S1 end is about 5 times higher than that of the S0 end [9]. Therefore, the energy deposit in each crystal can be measured two times independently for most of events, which is helpful to improve the energy resolution by combining the readouts from two ends. When the energy deposit in a BGO crystal is larger than the maximum measurable limit of S0 end, the energy deposit can still be properly reconstructed by the readout of S1 end after the attenuation correction [32]. However, when the energy deposit in one crystal is even larger than the maximum measurable limit of the S1 end, this event is defined as saturated and the energy information of this particular crystal is lost.

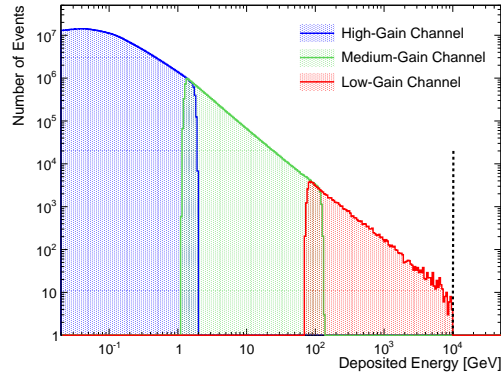


Figure 1: A typical energy deposit spectrum reconstructed from the S1 end of one BGO crystal. The blue, green and red histograms correspond to the high-gain (Dy8), medium-gain (Dy5), and low-gain (Dy2) ranges, respectively. The vertical black line represents the upper limit of the measurement.

Fig.1 shows a typical energy deposit spectrum reconstructed from the S1 end of one BGO crystal after the attenuation correction. A smooth transition between adjacent gain ranges can be clearly seen. The vertical black dashed line represents the upper measurement limit of the Dy2 readout channel, which is

$\sim 10$  TeV. As different PMTs have different gains [15], the upper measurement limit of the S1 end varies from  $\sim 4$  TeV to  $\sim 15$  TeV. This upper limit is high enough for the measurement of  $e^\pm/\gamma$  to energies of  $\sim 10$  TeV. However, for CR nuclei which are expected to be measured above energies of 100 TeV, the deposited energy in the calorimeter would exceed several tens of TeV, with the maximum energy in one single BGO bar exceeding several TeV. Therefore the saturation may appear for those very-high-energy events. Fig.2 shows a helium event with saturation. The deposited energy is 49.4 TeV before correction. The actual deposited energy of this event should be much larger.

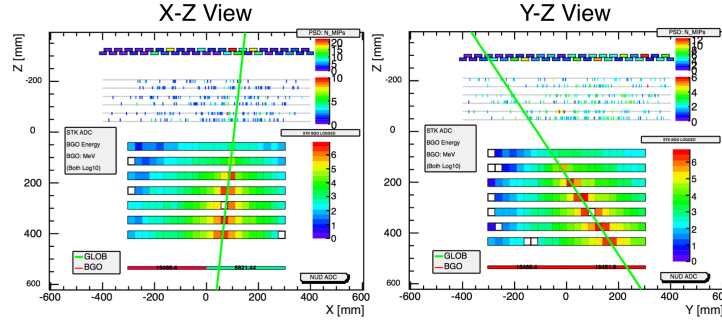


Figure 2: An illustration of a helium event with BGO readout saturation. The pre-correction total energy deposit is 49.4 TeV. The two empty BGO crystals on the shower axis are saturated, while the other empty crystals on the edge of shower are the ones without any deposited energy (or, the energy deposit is smaller than the noise threshold).

### 3. Method for the saturation correction

The saturation effect of the BGO readout has been taken into account in Monte Carlo (MC) simulation tool of DAMPE via importing saturation thresholds in the digitization procedure [33]. In this analysis, we use the protons and helium nuclei sample generated with the FTFP\_BERT hadronic interaction physics list in the Geant4 software [34]. Fig.3 shows the ratios of digitized energy deposits ( $E_{\text{digi}}$ ) to simulated energy deposits ( $E_{\text{simu}}$ ) for MC protons (left) and helium nuclei (right) with incident energies  $\geq 10$  TeV. The scattered

points below 1 represent events that suffered from the readout saturation effect. The fraction of saturated events becomes higher with the increase of particle energies. Particularly, at 100 TeV of incident energy, the fraction of saturated events is  $\sim 1.5\%$  ( $\sim 1.2\%$ ) for MC proton (helium). Therefore, the saturation effect would be more and more important for spectral measurements of CRs at increasingly high energies.

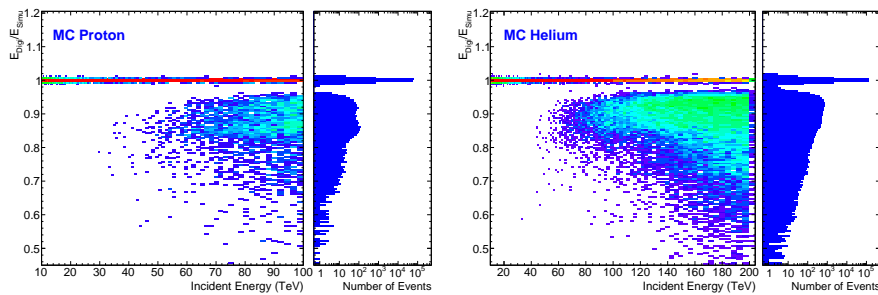


Figure 3: The ratios of digitized energy deposit to simulated energy deposit versus the incident energy for MC protons (left) and helium nuclei (right).

For the flight data, there would be one or more saturated BGO crystal(s) for a single event, leading to a large discrepancy for energy measurement. Since we have lost the energy information of the saturated crystal, we need to estimate its energy deposit based on the other un-saturated crystals and the shower development information. By combining the energy information of neighbouring BGO crystals, we propose a two-step correction method to reconstruct the energy deposit(s) of the saturated crystal(s).

### 3.1. Left-right correction

The simulations indicate that the saturated crystal should be the one with the maximum deposited energy in a certain BGO layer. As a prime estimation, we construct a correction variable  $\eta_{LR}$  based on the energies in the **left** and **right** neighbouring bars (see Fig.4), defined as follows:

$$\eta_{LR,j} = \frac{E_{Max,j}}{E_{Max,j} + E_{Left,j} + E_{Right,j}}, \quad (1)$$

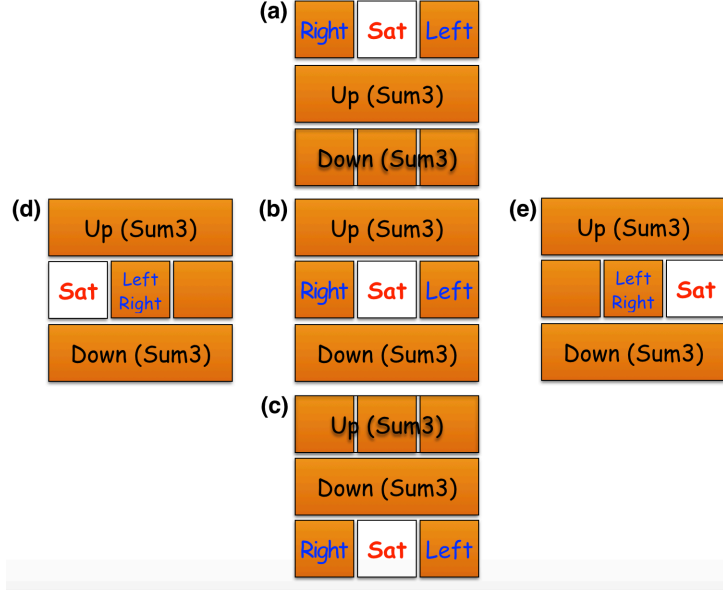


Figure 4: Classifications of events that need corrections: (a) for the top layer ( $j = 1$ ); (b) for middle layers ( $j = 2, \dots, 13$ ); (c) for the bottom layer ( $j = 14$ ); (d) for saturated bar on the left edge; (e) for saturated bar on the right edge.

where  $E_{\text{Max},j}$  is the maximum energy deposit in the  $j$ th layer,  $E_{\text{Left},j}$  ( $E_{\text{Right},j}$ ) is the energy deposit in its left (right) neighbouring crystal. When the saturated bar is located on the edge of one layer (classes (d) and (e) in Fig.4),  $E_{\text{Right},j}$  or  $E_{\text{Left},j}$  are counted twice.

From the simulation data, we obtain the  $\eta_{\text{LR}}$  distribution of each layer respectively. In the left panel of Fig.5, the  $\eta_{\text{LR},8}$  distribution of the 8th BGO layer versus the layer energy for MC helium events is shown as an illustration. The profile can be fitted with an empirical function:  $\eta_{\text{LR},j} = p_0 + p_1/\log(E_{\text{layer},j}/\text{GeV}) + p_2 \cdot \log(E_{\text{layer},j}/\text{GeV})$ , where  $E_{\text{layer},j}$  is the sum of energy deposits in all crystals of the  $j$ th layer. The parameters  $p_0$ ,  $p_1$  and  $p_2$  of each layer are obtained respectively. Moreover, the parameters for different nuclei, e.g. protons and helium nuclei, are obtained individually based on corresponding MC simulations.

Given the fact that the saturated crystal is the one with the maximum energy

deposit in its layer, the  $\eta_{\text{LR},j}$  can be applied for saturation correction. Since the energy information of the saturated crystal is totally lost, we firstly presume an initial estimation of  $E_{\text{Sat},j} = 5.5 \cdot (E_{\text{Left},j} + E_{\text{Right},j})$  to calculate the  $E_{\text{layer},j}$ . After that, we obtain  $\eta_{\text{LR},j}$  as the relation function of  $E_{\text{layer},j}$ . With  $\eta_{\text{LR},j}$ , the energy deposit in the saturated crystal would be corrected as:

$$E_{\text{Sat},j} = \frac{\eta_{\text{LR},j}}{1 - \eta_{\text{LR},j}} \cdot (E_{\text{Left},j} + E_{\text{Right},j}), \quad (2)$$

With the updated  $E_{\text{Sat},j}$ , we re-calculate  $E_{\text{layer},j}$  and  $\eta_{\text{LR},j}$ , and then apply Eq.(2) once more to obtain a better estimation of  $E_{\text{Sat},j}$ . For the case of more than one saturated crystals in a single shower, but existing in different layers, the correction can be performed independently for each layer. The **left-right** correction is taken as the first step for the following **up-down** global correction.

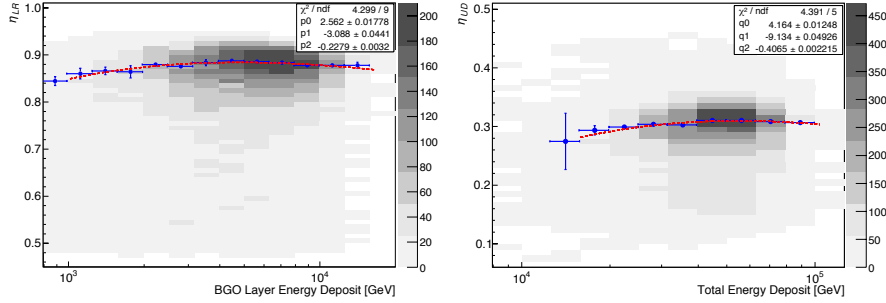


Figure 5: The profiles of  $\eta_{\text{LR}}$  of the 8th BGO layer versus the layer energy (**left**) and  $\eta_{\text{UD}}$  of the 8th BGO layer versus the total deposited energy (**right**) for MC helium events. The blue points and the error bars represent the fitted MPVs (most probable values) in each energy bin and their uncertainties ( $\pm\sigma$ ) from the fit using a local gaussian function.

### 3.2. Up-down correction

After the **left-right** correction, we obtain a prime energy estimation of the saturated crystal. However, to obtain a more precise energy deposit, we need to further take into account the longitudinal shower development. By considering the energy deposits of up and down layers, we construct another variable  $\eta_{\text{UD}}$ ,

defined as

$$\eta_{\text{UD},j} = \frac{E_{\text{Max},j}}{E_{\text{Max},j} + E_{\text{Left},j} + E_{\text{Right},j} + E_{\text{Up},j} + E_{\text{Down},j}}. \quad (3)$$

There are three types of definitions of  $E_{\text{Up},j}$  and  $E_{\text{Down},j}$ , corresponding to classes (a), (b), and (c) in Fig.4). For case (a),  $E_{\text{Up},j}$  is defined as the sum of the maximum bar energy and the energy deposits in its left and right neighbouring bars (Sum3 for short) of the second layer, while  $E_{\text{Down},j}$  is defined as the Sum3 of the third layer. For case (b),  $E_{\text{Up},j}$  is defined as the Sum3 of the layer  $j - 1$ , and  $E_{\text{Down},j}$  is defined as the Sum3 of the layer  $j + 1$ . For case (c),  $E_{\text{Up},j}$  is the Sum3 of layer 12, and  $E_{\text{Down},j}$  is the Sum3 of layer 13. As an illustration, the right panel of Fig.5 shows  $\eta_{\text{UD},8}$  versus the total deposited energy  $E_{\text{dep}}$  for the MC helium events. We also use the empirical form,  $\eta_{\text{UD},j} = q_0 + q_1 / \log(E_{\text{dep}}/\text{GeV}) + q_2 \cdot \log(E_{\text{dep}}/\text{GeV})$ , where  $E_{\text{dep}}$  is the total energy deposit in the calorimeter. As well, the parameters  $q_0$ ,  $q_1$  and  $q_2$  are obtained individually for different layers and for different nuclei.

With the prime energy estimation of each saturated crystal after the **left-right** correction, we obtain a prime estimation of the total energy deposit  $E_{\text{dep}}$ , which is the sum of energy deposits in all crystals including the saturated one(s). By  $E_{\text{dep}}$ , we obtain  $\eta_{\text{UD},j}$  for a further correction:

$$E_{\text{Sat},j} = \frac{\eta_{\text{UD},j}}{1 - \eta_{\text{UD},j}} \times (E_{\text{Left},j} + E_{\text{Right},j} + E_{\text{Up},j} + E_{\text{Down},j}). \quad (4)$$

If more than one saturated crystals exist in different layers, they would be corrected one by one globally. The correction of Eq.(4) can be performed iteratively, with updated  $E_{\text{Sat},j(s)}$  and  $E_{\text{dep}}$ . The results converge quickly after few iterations (three times in application).

#### 4. Performance

The performance of this two-step correction method is illustrated in Fig.6 using high energy MC helium nuclei. The Fig.6(a) shows the ratio of the corrected energy deposit ( $E_{\text{cor}}$ ) to the simulated one ( $E_{\text{simu}}$ ). The result proves

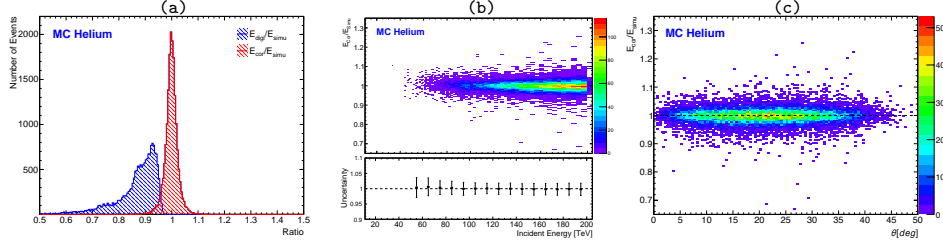


Figure 6: The performance of the correction method of MC saturated helium nuclei with incident energies above 10 TeV. (a): The distributions of  $E_{\text{digi}}/E_{\text{simu}}$  (blue) and  $E_{\text{cor}}/E_{\text{simu}}$  (red). (b): The  $E_{\text{cor}}/E_{\text{simu}}$  ratio versus incident energy and the uncertainties ( $\pm 1\sigma$ ) from the correction. (c): The  $E_{\text{cor}}/E_{\text{simu}}$  ratio versus incident zenith angle  $\theta$ .

that this method can well correct the energy deposits of saturated events. The  $E_{\text{cor}}/E_{\text{simu}}$  ratios for different incident energies of MC helium data are shown in Fig.6(b). We find that the performance of the correction is effective for all energies up to 200 TeV, and the uncertainty due to the correction is  $\sim 2\%$ . In this correction method, we do not further explore the parameterizations of the correction variables, i.e.  $\eta_{\text{LR}}$  and  $\eta_{\text{LR}}$ , by considering the dependence on the incident trajectory. For one reason, the wide distributions of the correction variables are primarily due to the randomness of the hadronic shower development, rather than the incident trajectory. For another, the correction variables only have an effective dependence on the hit position for on-axis events with a small incident zenith angle, however, the accepted particles of DAMPE are mostly oblique-incident with a zenith angle varying from 0 to 50 degree. As shown in Fig.6(c), the correction is actually independent with the incident zenith angle.

To validate the correction method with the flight data, we select high energy proton and helium candidates which are not saturated but close to the upper limit (see Fig.1). We require that the events should have at least one BGO crystal with energy deposits higher than  $0.8 \times E_{\text{thr}}$ , where  $E_{\text{thr}}$  represents the measurement threshold of the corresponding crystal. Then we artificially remove the energy deposit(s) of such BGO crystal(s) to produce pseudo saturated events. The performances of the correction for the pseudo saturated proton

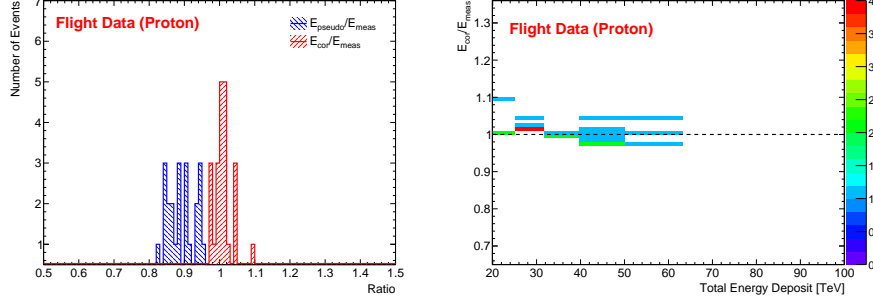


Figure 7: **Left:** The distributions of  $E_{\text{pseudo}}/E_{\text{meas}}$  (blue) and  $E_{\text{cor}}/E_{\text{meas}}$  (red) for pseudo saturated proton candidates with total energy deposits above 20 TeV. **Right:** The  $E_{\text{cor}}/E_{\text{meas}}$  ratio versus total energy deposit for pseudo saturated proton candidates in the flight data.

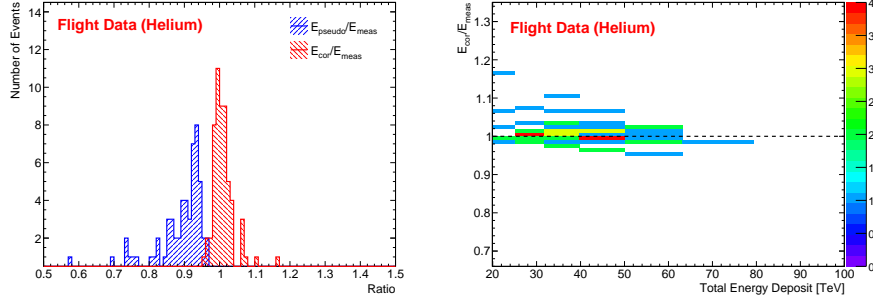


Figure 8: **Left:** The distributions of  $E_{\text{pseudo}}/E_{\text{meas}}$  (blue) and  $E_{\text{cor}}/E_{\text{meas}}$  (red) for pseudo saturated helium candidates with total energy deposits above 20 TeV. **Right:** The  $E_{\text{cor}}/E_{\text{meas}}$  ratio versus total energy deposit for pseudo saturated helium candidates in the flight data.

candidates and helium candidates are shown in Fig.7 and Fig.8, respectively. Despite the limited statistics, exported results indicate that the  $E_{\text{cor}}/E_{\text{meas}}$  ratio shows a good independence with the total energy deposit. For most of the pseudo saturated events, the energy deposit is properly corrected with respect to the measured one. However, it shows that a few events are slightly over-corrected. This happens because the pseudo saturated events are all under the saturation threshold, but the parameters we used for the corrections are derived with real saturated MC protons and heliums separately.

Finally in Fig.9 we show the comparisons among digitized (with saturation),

corrected, and simulated energies for MC protons and helium nuclei. As can be seen in this plot, the saturation effect becomes more and more important with the increase of incident energy above 50 TeV. The correction is thus necessary for the calculation of the energy response matrix which is relevant to the spectral measurements of CR nuclei. For the proton spectrum analysis up to 100TeV in Ref. [21], the correction has been applied for rare saturated proton candidates in the flight data.

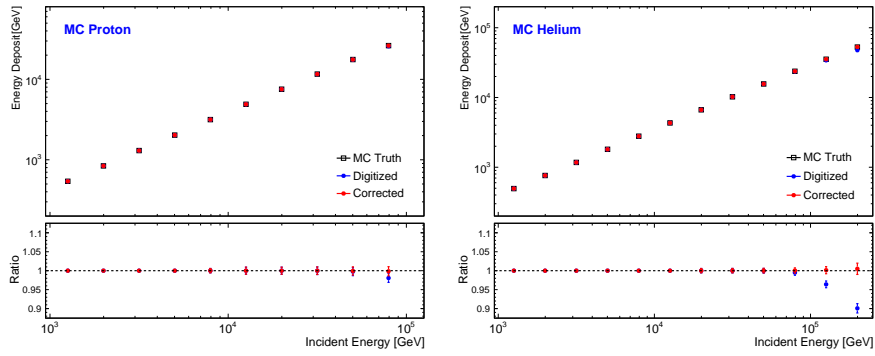


Figure 9: The digitized energies (blue dots) and corrected energies (red dots) compared with the incident energies (black squares) for MC protons (**left**) and helium nuclei (**right**). The bottom panels show the ratios of  $E_{digi}/E_{simu}$  (blue dots) and  $E_{cor}/E_{simu}$  (red dots).

## 5. Conclusions

In order to extend the energy measurements of the DAMPE for hadronic CRs to sub-PeV energy ranges, the BGO readout saturation effect has been studied based on detailed MC simulation data. Through combining the energy information of neighbouring BGO crystals and the longitudinal shower development, we proposed a two-step correction method to reconstruct the energy deposit of saturated crystals. The first step is to use the **left** and **right** energy deposits of the saturated crystal to get a prime estimation of the saturated crystals. Then the longitudinal shower development is further taken into account to improve the correction. The correction parameters are obtained for different

nucleonic species. The performance of the correction method is illustrated using MC helium nuclei and also helium candidates in flight data, which show that the energy deposits of saturated crystals can be well reconstructed. The correction is expected to be very helpful in the measurements of the CR spectra at very high energies.

One caveat of the correction method is that it applies only for the case with no adjacent saturated crystals within the same layer. The events with two or more adjacent crystals of the same layer get saturated are very rare, but existing in the flight data. The correction for such events would be more complicated and uncertain. We leave such a study in future works.

## 6. *Acknowledgments.*

This work is supported by the National Key Research and Development Program of China (Grant No. 2016YFA0400200), and the National Natural Science Foundation of China (Grant Nos. 11722328, 11773085, U1738205, U1738207, 11851305), and the 100 Talents Program of Chinese Academy of Sciences.

## References

- [1] A. W. Strong, I. V. Moskalenko, V. S. Ptuskin, Cosmic-ray propagation and interactions in the Galaxy, *Ann. Rev. Nucl. Part. Sci.* 57 (2007) 285–327. [arXiv:astro-ph/0701517](#), [doi:10.1146/annurev.nucl.57.090506.123011](#).
- [2] E. Amato, P. Blasi, Cosmic ray transport in the Galaxy: A review, *Adv. Space Res.* 62 (2018) 2731–2749. [arXiv:1704.05696](#), [doi:10.1016/j.asr.2017.04.019](#).
- [3] S. Gabici, C. Evoli, D. Gaggero, P. Lipari, P. Mertsch, E. Orlando, A. Strong, A. Vittino, The origin of Galactic cosmic rays: challenges to the standard paradigm, *Int. J. Mod. Phys. D* 28 (15) (2019) 1930022. [arXiv:1903.11584](#), [doi:10.1142/S0218271819300222](#).

- [4] M. Aguilar, et al., Observation of the Identical Rigidity Dependence of He, C, and O Cosmic Rays at High Rigidities by the Alpha Magnetic Spectrometer on the International Space Station, *Phys. Rev. Lett.* 119 (25) (2017) 251101. doi:10.1103/PhysRevLett.119.251101.
- [5] Y. Yoon, et al., Proton and Helium Spectra from the CREAM-III Flight, *Astrophys. J.* 839 (1) (2017) 5. arXiv:1704.02512, doi:10.3847/1538-4357/aa68e4.
- [6] E. Atkin, et al., New Universal Cosmic-Ray Knee near a Magnetic Rigidity of 10 TV with the NUCLEON Space Observatory, *JETP Lett.* 108 (1) (2018) 5–12. arXiv:1805.07119, doi:10.1134/S0021364018130015.
- [7] O. Adriani, et al., Direct Measurement of the Cosmic-Ray Proton Spectrum from 50 GeV to 10 TeV with the Calorimetric Electron Telescope on the International Space Station, *Phys. Rev. Lett.* 122 (18) (2019) 181102. arXiv:1905.04229, doi:10.1103/PhysRevLett.122.181102.
- [8] J. Chang, Dark Matter Particle Explorer: The First Chinese Cosmic Ray and Hard  $\gamma$ -ray Detector in Space, *Chinese Journal of Space Science* 34 (5) (2014) 550–557.
- [9] J. Chang, et al. (DAMPE Collaborabtion), The DArk Matter Particle Explorer mission, *Astropart. Phys.* 95 (2017) 6–24. doi:10.1016/j.astropartphys.2017.08.005.
- [10] Y. Yu, et al., The plastic scintillator detector for DAMPE, *Astropart. Phys.* 94 (2017) 1–10. arXiv:1703.00098, doi:10.1016/j.astropartphys.2017.06.004.
- [11] M. Ding, et al., Calibration of the DAMPE Plastic Scintillator Detector and its on-orbit performance, *Res. Astron. Astrophys.* 19 (3) (2019) 047. arXiv:1810.09901, doi:10.1088/1674-4527/19/3/47.
- [12] P. Azzarello, et al., The DAMPE silicon–tungsten tracker, *Nucl. Instrum. Meth. A* 831 (2016) 378–384. doi:10.1016/j.nima.2016.02.077.

- [13] A. Tykhonov, et al., In-flight performance of the DAMPE silicon tracker, *Nucl. Instrum. Meth. A* 924 (2019) 309–315. [arXiv:1806.10355](#), doi:10.1016/j.nima.2018.06.036.
- [14] Y.-L. Zhang, et al., A high dynamic range readout unit for a calorimeter, *Chin. Phys. C* 36 (2012) 71–73.
- [15] Z. Zhang, et al., The calibration and electron energy reconstruction of the BGO ECAL of the DAMPE detector, *Nucl. Instrum. Meth. A* 836 (2016) 98–104. doi:10.1016/j.nima.2016.08.015.
- [16] Y.-Y. Huang, T. Ma, C. Yue, Y. Zhang, J. Chang, T.-K. Dong, Y.-Q. Zhang, Calibration and performance of the neutron detector onboard of the DAMPE mission, *Res. Astron. Astrophys.* 20 (9) (2020) 153. [arXiv:2005.07828](#), doi:10.1088/16744527/20/9/153.
- [17] A. Tykhonov, et al., Internal alignment and position resolution of the silicon tracker of DAMPE determined with orbit data, *Nucl. Instrum. Meth. A* 893 (2018) 43–56. [arXiv:1712.02739](#), doi:10.1016/j.nima.2018.02.105.
- [18] P.-X. Ma, et al., A method for aligning the plastic scintillator detector on DAMPE, *Res. Astron. Astrophys.* 19 (6) (2019) 082. [arXiv:1808.05720](#), doi:10.1088/1674-4527/19/6/82.
- [19] T. Dong, et al., Charge measurement of cosmic ray nuclei with the plastic scintillator detector of DAMPE, *Astropart. Phys.* 105 (2019) 31–36. [arXiv:1810.10784](#), doi:10.1016/j.astropartphys.2018.10.001.
- [20] G. Ambrosi, et al. (DAMPE Collaborabtion), Direct detection of a break in the teraelectronvolt cosmic-ray spectrum of electrons and positrons, *Nature* 552 (2017) 63–66. [arXiv:1711.10981](#), doi:10.1038/nature24475.
- [21] Q. An, et al. (DAMPE Collaborabtion), Measurement of the cosmic-ray proton spectrum from 40 GeV to 100 TeV with the DAMPE satellite, *Sci. Adv.* 5 (9) (2019) eaax3793. [arXiv:1909.12860](#), doi:10.1126/sciadv.aax3793.

- [22] Q. Yuan, et al., Interpretations of the DAMPE electron data, preprint [arXiv:1711.10989](https://arxiv.org/abs/1711.10989).
- [23] X. Pan, C. Zhang, L. Feng, Interpretation of the DAMPE 1.4 TeV peak according to the decaying dark matter model, *Sci. China Phys. Mech. Astron.* 61 (10) (2018) 101006. doi:[10.1007/s11433-018-9257-3](https://doi.org/10.1007/s11433-018-9257-3).
- [24] Q. Yuan, L. Feng, Dark Matter Particle Explorer observations of high-energy cosmic ray electrons plus positrons and their physical implications, *Sci. China Phys. Mech. Astron.* 61 (10) (2018) 101002. [arXiv:1807.11638](https://arxiv.org/abs/1807.11638), doi:[10.1007/s11433-018-9226-y](https://doi.org/10.1007/s11433-018-9226-y).
- [25] C. Yue, et al., Implications on the origin of cosmic rays in light of 10 TV spectral softenings, *Front. Phys. (Beijing)* 15 (2) (2020) 24601. [arXiv:1909.12857](https://arxiv.org/abs/1909.12857), doi:[10.1007/s11467-019-0946-8](https://doi.org/10.1007/s11467-019-0946-8).
- [26] Z.-L. Xu, et al., An algorithm to resolve  $\gamma$ -rays from charged cosmic rays with DAMPE, *Res. Astron. Astrophys.* 18 (3) (2018) 027. [arXiv:1712.02939](https://arxiv.org/abs/1712.02939), doi:[10.1088/1674-4527/18/3/27](https://doi.org/10.1088/1674-4527/18/3/27).
- [27] K.-K. Duan, et al., DmpIRFs and DmpST: DAMPE Instrument Response Functions and Science Tools for Gamma-Ray Data Analysis, *Res. Astron. Astrophys.* 19 (9) (2019) 132. [arXiv:1904.13098](https://arxiv.org/abs/1904.13098), doi:[10.1088/1674-4527/19/9/132](https://doi.org/10.1088/1674-4527/19/9/132).
- [28] X. Li, K. Duan, W. Jiang, Z. Shen, M. Munoz Salinas, Recent Gamma-ray Results from DAMPE, in: 36th International Cosmic Ray Conference (ICRC2019), Vol. 36 of International Cosmic Ray Conference, 2019, p. 576.
- [29] Z. Zhang, et al., Design of a high dynamic range photomultiplier base board for the BGO ECAL of DAMPE, *Nucl. Instrum. Meth. A* 780 (2015) 21–26. doi:[10.1016/j.nima.2015.01.036](https://doi.org/10.1016/j.nima.2015.01.036).
- [30] G. Ambrosi, et al. (DAMPE Collaborabtion), The on-orbit calibration of DArK Matter Particle Explorer, *Astropart. Phys.* 106 (2019) 18–34. [arXiv:1907.02173](https://arxiv.org/abs/1907.02173), doi:[10.1016/j.astropartphys.2018.10.006](https://doi.org/10.1016/j.astropartphys.2018.10.006).

- [31] A. Kounine, Z. Weng, W. Xu, C. Zhang, Precision measurement of 0.5 GeV – 3 TeV electrons and positrons using the AMS Electromagnetic Calorimeter, *Nucl. Instrum. Meth. A* 869 (2017) 110–117. doi:10.1016/j.nima.2017.07.013.
- [32] L. Wu, et al., Calibration and Status of the 3-D Imaging Calorimeter of DAMPE for Cosmic Ray Physics on Orbit, *IEEE Transactions on Nuclear Science* 65 (8) (2018) 2007–2012. doi:10.1109/TNS.2018.2814619.
- [33] C. Yue, et al., A parameterized energy correction method for electromagnetic showers in BGO-ECAL of DAMPE, *Nuclear Instruments and Methods in Physics Research A* 856 (2017) 11–16. arXiv:1703.02821, doi:10.1016/j.nima.2017.03.013.
- [34] J. Allison, et al., Recent developments in Geant4, *Nucl. Instrum. Meth. A* 835 (2016) 186–225. doi:10.1016/j.nima.2016.06.125.